Cancer Research

A PET Imaging Strategy to Visualize Activated T Cells in Acute Graft-versus-Host Disease Elicited by Allogenic Hematopoietic Cell Transplant

John A. Ronald[1,2,3,4], Byung-Su Kim[5], Gayatri Gowrishankar[1,2], Mohammad Namavari[1,2], Israt S. Alam[1,2], Aloma D'Souza[1,2], Hidekazu Nishikii[5], Hui-Yen Chuang[1,6], Ohad Ilovich[1,2], Chih-Feng Lin[1,7,8], Robert Reeves[1,2], Adam Shuhendler[1,2], Aileen Hoehne[1,2], Carmel T. Chan[1,2], Jeanette Baker[5], Shahriar S. Yaghoubi[9], Henry F. VanBrocklin[10], Randall Hawkins[10], Benjamin L. Franc[10], Salma Jivan[10], James B. Slater[10], Emily F. Verdin[10], Kenneth T. Gao[10], Jonathan Benjamin[5], Robert Negrin[5], and Sanjiv Sam Gambhir[1,2]

Abstract

A major barrier to successful use of allogeneic hematopoietic cell transplantation is acute graft-versus-host disease (aGVHD), a devastating condition that arises when donor T cells attack host tissues. With current technologies, aGVHD diagnosis is typically made after end-organ injury and often requires invasive tests and tissue biopsies. This affects patient prognosis as treatments are dramatically less effective at late disease stages. Here, we show that a novel PET radiotracer, 2′-deoxy-2′-[18F]fluoro-9-β-D-arabinofuranosylguanine ([18F]F-AraG), targeted toward two salvage kinase pathways preferentially accumulates in activated primary T cells. [18F]F-AraG PET imaging of a murine aGVHD model enabled visualization of secondary lymphoid organs harboring activated donor T cells prior to clinical symptoms. Tracer biodistribution in healthy humans showed favorable kinetics. This new PET strategy has great potential for early aGVHD diagnosis, enabling timely treatments and improved patient outcomes. [18F]F-AraG may be useful for imaging activated T cells in various biomedical applications. *Cancer Res; 77(11); 2893–902. ©2017 AACR.*

Introduction

Allogeneic hematopoietic cell transplantation (HCT) is increasingly being used as a potentially curative treatment for hematologic malignancies and other life-threatening diseases (1). In malignancy treatment, HCT can destroy residual tumor cells that persist after other treatments, an effect called the graft-versus-tumor (GVT) reaction. The two most important causes of nonrelapse mortality are infections and acute graft-versus-host disease (aGVHD; ref. 2). Although infections can be successfully treated, at the time of diagnosis, aGVHD patients are less responsive to current treatments. Thus, the challenge for widespread adoption of HCT is either avoidance or better management of aGVHD, but arguably the diagnosis and treatment of this devastating disease has only marginally improved in the last 20 years.

aGVHD is an immunological disorder where donor $CD4^+$ and $CD8^+$ T cells migrate to secondary lymphoid organs and are activated by innate immune cells that become reactive by the conditioning therapy for HCT (1). These alloreactive donor T cells then undergo massive proliferation and home to various organs [gastrointestinal (GI) tract, liver, and skin] and attack host cells via direct cytolysis or cytokine production causing a wide range of symptoms (3). Incidence rates are approximately 20% to 50% for patients receiving HLA-matched-related donor transplants and incidence and severity of aGVHD increases according to HLA disparity (4). Overall grade is known to have a major effect on patient outcome, with grade I or II cases associated with little morbidity and mortality, and grade III or IV cases associated with high mortality (5). Because long-term survival of grade III and IV aGVHD is a dismal 10% to 20% (6), it is important to detect patients who will progress to high-grade aGVHD earlier in their course. Dramatic differences in response rate with disease stage have been reported including 63% to 95% for grade II, 17% to 30% for grade III, and 0% to 6% for grade IV patients (7). Unfortunately, early aGVHD diagnosis is difficult due to its nonspecific symptoms and numerous differential diagnoses (8), and typically a diagnosis occurs when overt symptoms such as skin, GI, or liver problems become apparent (9). Invasive endoscopic-guided biopsy (often from liver or GI tract) is required to confirm an aGVHD (4), but bleeding tendency and critical

[1]Molecular Imaging Program at Stanford, Stanford University, Stanford, California. [2]Department of Radiology, Stanford University School of Medicine, Stanford, California. [3]Robarts Research Institute, Department of Medical Biophysics, The University of Western Ontario, London, Ontario, Canada. [4]Lawson Health Research Institute, London, Ontario, Canada. [5]Division of Blood and Marrow Transplantation, Department of Medicine, Stanford University, Stanford, California. [6]Department of Biomedical Imaging and Radiological Sciences, National Yang-Ming University, Taipei, Taiwan. [7]Department of Otolaryngology Head and Neck Surgery, National Taiwan University Hospital, Taipei, Taiwan. [8]Graduate Institute of Pathology, National Taiwan University College of Medicine, Taipei, Taiwan. [9]Cellsight Technologies Incorporated, San Francisco, California. [10]Department of Radiology and Biomedical Imaging, University of California, San Francisco, San Francisco, California.

Note: Supplementary data for this article are available at Cancer Research Online (http://cancerres.aacrjournals.org/).

J.A. Ronald and B.-S. Kim contributed equally to this article.

Corresponding Author: Sanjiv Sam Gambhir, Department of Radiology, Molecular Imaging Program at Stanford, Stanford University, Stanford, CA 94305. Phone: 650-723-8649; E-mail: sgambhir@stanford.edu

doi: 10.1158/0008-5472.CAN-16-2953

illness associated with HCT make it near impossible to perform these procedures. Blood biomarkers are under active investigation, but to date, no biomarker has been validated for early aGVHD diagnosis (10, 11). These critical issues dramatically delay the onset and effectiveness of potentially life-saving pre-emptive or early treatment interventions. Thus, noninvasive methods that can diagnose aGVHD at earlier stages are urgently needed but entirely lacking. An imaging method that can quantitatively track alloreactive donor T-cell dynamics and stratify the risk of aGVHD prior to overt symptoms could provide an ideal solution.

PET has several key strengths including high sensitivity (10^{-9} to 10^{-12} mol/L), quantitative capability, and limitless depth of penetration (12). To date, few PET radiotracers have been developed for imaging the immune system and even fewer for specific imaging of distinct immune cell types such as activated T cells (13–15). Our group recently developed the radiotracer 2′-deoxy-2′-[^{18}F]fluoro-9-β-D-arabinofuranosyl guanine ([^{18}F]F-AraG) (Supplementary Fig. S1A; ref. 16). [^{18}F]F-AraG is an analog of arabinosyl guanine (AraG), a compound identified to have specific cytotoxicity toward T-lymphocyte and T-lymphoblastoid cells versus other immune cell types (17–19). Nelarabine, the water-soluble AraG prodrug, is indicated for the treatment of patients with refractory/relapsed T-cell acute lymphoblastic leukemia (T-ALL) and T-cell lymphoblastic lymphoma (T-LBL; ref. 20). AraG enters cells via one of two nucleoside transporters followed by the initial and rate-limiting phosphorylation of AraG to AraG-monophosphate (AraGMP) by either cytosolic deoxycytidine kinase (dCK) or mitochondrial deoxyguanosine kinase (dGK; Supplementary Fig. S1B; refs. 20, 21). Continued phosphorylation to AraG-triphosphate (AraGTP) can inhibit DNA synthesis and induce cytotoxic effects specifically in T-lymphocyte and T-lymphoblastoid cells (18, 20). Thus, [^{18}F]F-AraG PET imaging may provide a novel method for imaging of activated T-cell dynamics in living subjects without toxicity because the tracer is given in very low (ng-μg) mass levels. This technology could allow clinicians to utilize existing or novel interventions in a timely fashion and to more effectively monitor the outcome of such treatments. The ultimate utility of such efforts would be to prevent progression to higher-grade disease and improve patient outcome.

Materials and Methods

Cell lines

Jurkat (ATCC), Ramos (ATCC), and Daudi (ATCC) cells were cultured in RPMI-1640 containing 10% FBS and 1x Antibiotic-Antimycotic (Anti-Anti) solution. For Ramos cells, the FBS was heat inactivated at 56°C for 30 minutes. HL-60 (ATCC) cells were cultured in Iscove's Modified Dulbecco's Medium containing 20% FBS and 1x Anti-Anti. CCRF-CEM (ATCC), Ara-C8D (dCK$^-$ or CCRF-CEM-dCK$^-$, a kind gift from Dr. Beverly Mitchell, Stanford University), Ara-C8D dCK$^+$ (dCK$^+$), and Ara-C8D dGK$^+$ (dGK$^+$; the latter two kind gifts from Dr. Varsha Gandhi, MD Anderson) were grown in low-glucose DMEM with 10% FBS. HeLa, MDA-MB-231 (ATCC) and PyMT (a kind gift from Dr. Heike Daldrup-Link, Stanford University) cells were maintained in DMEM containing 10% FBS and 1x Anti-Anti. MeWo (ATCC) cells were maintained in MEM containing 10% FBS and 1x Anti-Anti. CHO-K1 cells (ATCC) were maintained in F-12K medium containing 10% FBS and 1x Anti-Anti. All cells routinely tested negative for mycoplasma using the MycoAlert mycoplasma detection Kit (Lonza; last testing: December 2014). All cell lines were used for experiments within a month of thawing, acquired from the various sources (primarily ATCC) between 2011 and 2014, and cell line authentication was not performed. All cells were maintained at 37°C in a humidified atmosphere containing 5% CO_2.

Tracers

AraG was purchased from R.I. Chemicals, Inc. Tritiated AraG ([^{3}H]AraG) and tritiated 1-(2-deoxy-2-fluoro-arabinofuranosyl)-cytosine ([^{3}H]F-AraC) were purchased from Moravek Biochemicals. [^{18}F]F-AraG was synthesized as previously described (16). [^{18}F]F-AraG for human imaging was prepared according to the approved IND Chemistry Manufacturing and Control (CMC) procedures using the Neptis perform PET synthesizer, a modification of the published procedure (16). The synthesis details are provided in Supplementary Information. Prior to injection in human subjects, the prepared [^{18}F]F-AraG passed all quality specifications.

Primary T-cell isolation and activation

Mouse primary T cells were isolated via FAC sorting from spleens of BALB/c mice (Charles River) using an APC-conjugated Anti-Mouse CD90.2 (Thy-1.2) antibody (eBioscience, Inc.). Purified T cells were maintained for 2 days in RPMI-1640 containing 10% FBS and 1% penicillin/streptomycin at an initial density of 1×10^6 cells/mL. For activation, cells were incubated with mouse T-Activator CD3/CD28 Dynabeads per the manufacturer's instructions (bead:cell ratio of 1:10; Life Technologies). Tracer uptake experiments were performed 48 hours after activation.

Human peripheral blood mononuclear cells (PBMC) were isolated from whole blood (obtained at the Stanford Blood Center) using Ficoll-Paque Plus following the manufacturer's instructions (GE Healthcare). T cells were isolated via magnetic-activated cell sorting using the Naïve Pan T Cell Isolation Kit per the manufacturer's instructions (Miltenyi Biotec). To assess successful purification (>90% T cells), both PBMCs and sorted cells were immunostained with a human CD3-FITC antibody (Miltenyi Biotec), and the percentage of CD3-positive cells was determined under a fluorescent microscope (EVOS FL cell imaging system, Life Technologies). T cells were activated with T-cell activation/expansion kit as per the manufacturer's instructions (Miltenyi Biotec). Tracer uptake experiments were performed 48 hours after activation.

Tracer uptake and efflux assays for immune cells

A total of 5×10^5 (primary mouse T cells), 2×10^6 (human primary T cells), or 1×10^6 (cell lines) cells in 1 mL of Hanks balanced salt solution (HBSS) were incubated with tracer (([^{18}F]F-AraG (5 μCi), [^{3}H]AraG (2 μCi), or [^{3}H]F-AraC (1 μCi)) for 1 hour to measure uptake. For competition assays, cells were incubated with or without 100 μmol/L AraG during tracer incubation (R.I. Chemical, Inc.). To assess tracer efflux (percentage retained), cells were centrifuged at 1,000 x *g* for 5 minutes after 1-hour tracer incubation, supernatant was aspirated, and cells were incubated in 1 mL of HBSS for an additional hour. To measure [^{18}F]F-AraG radioactivity within cells, we used a method previously described (22). Briefly, 400 μL of cell suspension was transferred onto 200 μL of an 88:12 silicon oil (density = 1.05) and mineral oil (density = 0.877) mixture and centrifuged at 10,000 rpm for 3 minutes. This enables efficient separation of

radioactivity in media and cell pellets. Tubes were frozen in liquid nitrogen, pellets were transferred to scintillation tubes, and radioactivity was measured using an automated γ counter (Cobra II; Packard). For [^{3}H]AraG or [^{3}H]F-AraC measurement, 20 μL of 2N KOH was layered under the oil mixture (23). Note that 40 μL of 1N HCl and 10 mL of scintillation liquid were added sequentially to cell pellets, and radioactivity was measured using an LS 6500 Multi-Purpose scintillation counter (Beckman Coulter). Using the remaining cell fraction, total cell number was determined using an automated cell counter (Nexcelom Bioscience). Data were expressed as percentage uptake per 10^5 cells.

aGVHD mouse model

All procedures performed on animals were approved by Stanford University's Institutional Animal Care and Use Committee and were within the guidelines of humane care of laboratory animals (Protocol #27293). Both control (n = 10) and aGVHD mice (n = 11) were generated as previously described (11, 24, 25). Briefly, recipient 8- to 16-week-old female BALB/c mice (Balb/cJ; 18–22 g; Jackson Laboratories) were irradiated with 800 cGy in two split doses on day 0 with an electron linear accelerator. T-cell–depleted bone marrow (TCD-BM) cells were obtained from wild-type 8- to 16-week-old female C57Bl/6 donor mice (control mice; C57Bl/6J; 18–22 g; Jackson Laboratories). Donor T cells were obtained from the spleens of firefly luciferase (Luc$^+$) 8- to 16-week-old female C57Bl/6-L2G85 (18–22 g) donor mice (11, 26). T-cell depletion and donor T-cell selection were performed using CD4 and CD8 magnetic beads (Miltenyi Biotec). All mice received intravenous injection of 5×10^6 TCD-BM cells to initiate hematopoietic reconstitution. For aGVHD mice, they also received 1×10^6 Luc$^+$ T cells coinjected with the TCD-BM cells. For visualization of donor-derived T cells in immunofluorescence experiments, 8- to 16-week-old female Luc$^+$*gfp*$^+$ C57Bl/6 mice (18–22 g) were used as the T-cell donor (27).

Bioluminescence imaging, PET, and tracer biodistribution studies

For bioluminescence imaging (BLI), mice were anesthetized and imaging was performed using an IVIS Spectrum cooled charge-coupled device imaging system (Perkin Elmer) 5 minutes after an intraperitoneal injection of the substrate D-luciferin (3 mg). Images were analyzed with Living Image Software 4.1 (Perkin Elmer).

For PET/CT imaging, mice were anesthetized and injected with approximately 200 μCi of [^{18}F]F-AraG via the lateral tail-vein. Sixty minutes after injection, static PET images (10-minute acquisition time) were collected using a microPET/CT hybrid Inveon scanner (Siemens). A CT image was acquired just before each PET scan to provide an anatomic reference frame for the respective PET data. All PET images were reconstructed with a three-dimensional ordered-subsets expectation maximization algorithm and coregistered with CT images using the Inveon Research Workplace image analysis software (version 4.0; Siemens). To quantify tracer uptake in PET images, three-dimensional regions of interest were drawn over the cervical lymph nodes (CLN), a 50% threshold was applied to each selected region, and partial volume-corrected uptake values were expressed as percentage injected dose per gram of tissue (%ID/g).

Ninety minutes after tracer administration, mice were euthanized, various tissues [blood, heart, small intestine, kidney, liver, lung, muscle, spleen, mesenteric lymph nodes (MLN), and CLN] were collected, weighed, and radioactivity was measured using an automated γ counter (Cobra II; Packard). Radioactivity was decay-corrected to the time of radiotracer injection using diluted aliquots of the initial administered dose as standards. Data are expressed as percentage injected dose per gram of tissue (%ID/g) values.

Imaging studies in humans

Six healthy volunteers (3 women, 3 men; 24–60 years old) were enrolled to study the whole-body kinetics of [^{18}F]F-AraG in humans (IND #123591) at the University of California, San Francisco, under protocols approved by the Institutional Review Board and the Radiation Safety Committee. The following subjects were excluded from participating in this study: pregnant or breastfeeding women, individuals with any type of chronic illness or symptoms of disease, individuals with known or suspected substance abuse, individuals unable or unwilling to comply with the study procedures, and individuals with contraindications to MRI. Written informed consents were obtained from the volunteers prior to the initiation of each imaging study. Details of image acquisition and analysis are provided in Supplementary Information.

Results

AraG selective cytotoxicity is related to the preferential ability of T lymphocytes or T-cell–derived cancer cells versus other immune cell types to retain AraGTP (19, 28). To evaluate the potential utility of [^{18}F]F-AraG, we first assessed uptake and retention across a number of immune cell lines that are all derived from patients with hematologic malignancies. Compared with T-cell and B lymphoblast cell lines, significantly increased and decreased tracer uptake at 1 hour was seen in myeloid and B lymphoblast cells, respectively ($P < 0.05$; Supplementary Fig. S2A). Importantly, both T-cell lines significantly and efficiently (∼100%) retained the tracer (expressed as percentage remaining in cells compared with tracer uptake at 1 hour) compared with all other immune cell lineages ($P < 0.001$; Supplementary Fig. S2B). We also assessed the uptake and retention of a tritiated version of another nucleoside analog radiotracer, 1-(2′-deoxy-2′-[^{18}F]fluoro-D-arabinofuranosyl) cytosine ([^{18}F]F-AraC, also called [^{18}F]FAC). [^{18}F]F-AraC, a substrate for dCK, shows higher uptake in proliferating versus resting T cells and may be useful for visualizing regions of immune activation *in vivo* with PET (13). We found significantly higher levels of [^{3}H]F-AraC uptake in T-lymphocyte cells versus all other immune cell lines, and significantly higher uptake in T lymphoblast line compared with B-cell lines ($P < 0.01$; Supplementary Fig. S2C). We also found less [^{18}F]F-AraC retention (<100%) in T cell lines versus [^{18}F]F-AraG, equivalent [^{18}F]F-AraC retention between T-lymphoblast, T-lymphocyte, and myeloid cell lines, significantly decreased retention in B cells versus T lymphoblasts, and significantly decreased retention in B versus T lymphocytes ($P < 0.05$; Supplementary Fig. S2D). Coincubation with molar excess of nonradiolabeled AraG (100 μmol/L) significantly impaired [^{18}F]F-AraG uptake across all cell types ($P < 0.05$; Supplementary Fig. S3). Significantly higher uptake was also seen across several solid tumor cell lines with [^{3}H]F-AraC versus [^{18}F]F-AraG ($P < 0.01$; Supplementary Fig. S4A), as well as significantly higher retention of [^{3}H]F-AraC in both cervical cancer and melanoma cell lines ($P < 0.01$; Supplementary Fig. S4B). Thus,

[^{18}F]F-AraG accumulates in cell lines in a manner that is similar to AraG but distinguishable from the AraC-based tracer.

We next evaluated whether [^{18}F]F-AraG accumulates in cells via dCK and/or dGK activity using established cell lines (21). Loss of dCK in mutant CCRF-CEM T-lymphoblast cells (dCK$^-$), as confirmed with Western blot analysis (Supplementary Fig. S5), significantly impaired [^{18}F]F-AraG uptake ($P < 0.001$; Fig. 1A). Overexpression of dCK (dCK$^+$) in dCK$^-$ cells showed a trend toward increased tracer uptake in dCK$^+$ compared with dCK$^-$ cells ($P = 0.17$), whereas dGK overexpression (dGK$^+$) in dCK$^-$ cells significantly ($P < 0.05$) increased tracer uptake in dGK$^+$ compared with dCK$^-$ cells (Fig. 1A). Uptake levels in dGK$^+$ cells were not significantly different to levels in wild-type CCRF-CEM cells. No effects on tracer retention were seen across any of these cell lines (Fig. 1B). dGK utilization of [^{18}F]F-AraG was further confirmed via significantly higher uptake and retention in CHO-K1 cells overexpressing dGK compared with empty vector–transfected cells ($P < 0.05$; Supplementary Fig. S6A and S6B). Similar studies with [^{3}H]F-AraC showed this tracer accumulated via dCK, but not dGK, and lack of dCK activity significantly reduced retention of the tracer ($P < 0.05$; Supplementary Fig. S7A and S7B). dCK overexpression had no significant effects on uptake or retention of [^{18}F]F-AraG in this cell type. Our evidence supports that in contrast to [^{18}F]F-AraC that accumulates via dCK alone, but in line with AraG metabolism (21), [^{18}F]F-AraG accumulates in cells via both dCK and dGK activities. These findings support recently published observations in a study on a novel PET tracer metabolized by dCK, which also noted a role of dGK in the metabolism of [^{18}F]F-AraG (29); however, we extend upon these previous findings to highlight the additional role of dCK activity in the metabolism of [^{18}F]F-AraG.

As our goal is to image activated primary T lymphocytes, not T-cell lines, uptake and retention of various tracers ([^{18}F]F-AraG, [^{3}H]AraG, and [^{3}H]AraC) in primary murine and human resting and activated T cells was also evaluated. Activated murine T cells (2 days after activation) appeared morphologically distinct (elongated vs. round) compared with resting cells (Supplementary Fig. S8A) and accumulated significantly higher (~7.8-fold) [^{18}F]F-AraG ($P < 0.001$; Supplementary Fig. S8B). A 2-day activation protocol of sorted (>90% CD3$^+$ T cells) human PBMCs resulted in similar morphologic changes as seen in murine T cells (Supplementary Fig. S9). Significantly higher uptake in activated versus resting cells was seen with both [^{3}H]AraG and [^{3}H]F-AraC, but retention in both cell states was significantly higher with [^{3}H]AraG ($P < 0.05$; Supplementary Fig. S10). Finally, we found significantly higher uptake (19-fold) of [^{18}F]F-AraG in activated versus resting human T cells ($P < 0.001$; Fig. 1C). Although [^{18}F]F-AraG significantly effluxed out of activated but not resting cells ($P < 0.05$), absolute levels in activated versus resting cells at all time points evaluated were significantly higher ($P < 0.01$). Overall, these results suggest the use of [^{18}F]F-AraG may allow selective PET imaging of activated versus resting T cells.

The ability to visualize sites of activated T-cell accumulation in aGVHD with [^{18}F]F-AraG PET imaging was assessed in a well-established MHC mismatch aGVHD mouse model (11, 24–26). In this model, donor T cells constitutively express the bioluminescence reporter gene firefly luciferase (Luc) enabling *in vivo* BLI to monitor sites of donor T-cell accumulation and proliferation over time. We performed *in vivo* BLI, [^{18}F]F-AraG PET/CT imaging, tracer biodistribution studies, and *ex vivo* immunofluorescence studies at both days 3 and 10 after model initiation in both control (irradiated and bone marrow–transplanted mice without

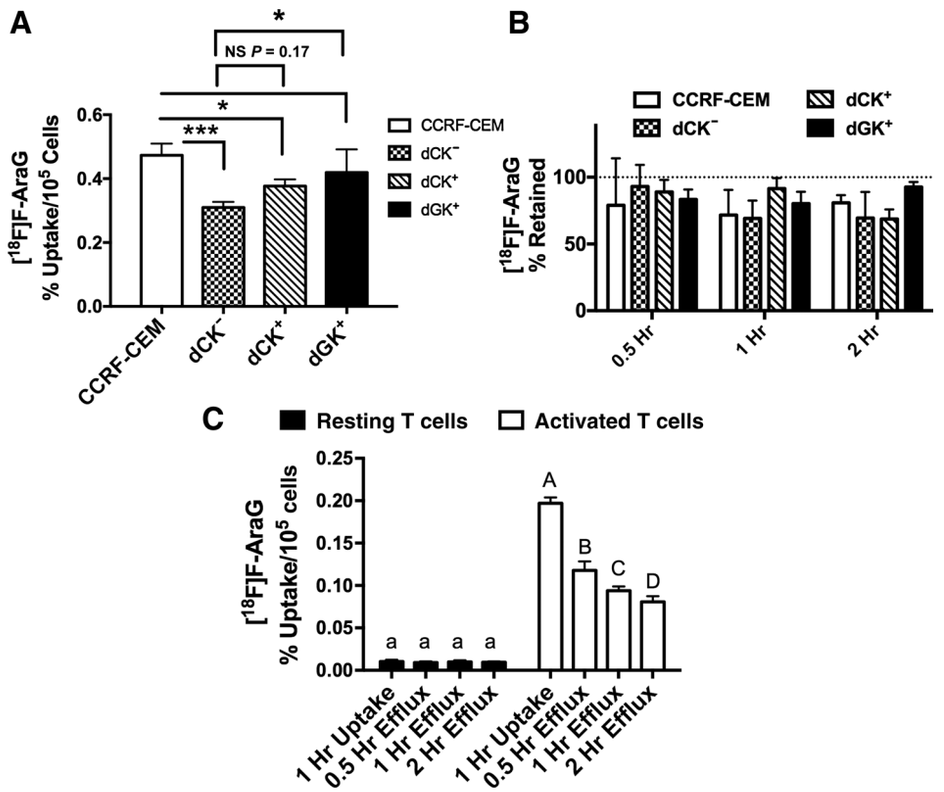

Figure 1.

[^{18}F]F-AraG accumulates in cells via dCK and dGK activity and at increased levels in activated versus resting primary human T cells. Uptake (**A**) and retention (**B**) of [^{18}F]F-AraG across wild-type CCRF-CEM T lymphoblasts, mutant CCRF-CEM dCK$^-$ cells (dCK$^-$), and dCK$^-$ cells overexpressing either dCK (dCK$^+$) or dGK (dGK$^+$; $n = 4$ per cell type per time point). Significantly less uptake was seen due to the loss of dCK in wild-type cells (CCRF-CEM vs. dCK$^-$; $P < 0.001$). There was a trend toward higher uptake in dCK$^+$ versus dCK$^-$ cells, whereas dGK$^+$ cells had significantly higher uptake compared with dCK$^-$ cells and equivalent uptake compared with wild-type cells. No differences in retention were seen across cell types. **C,** Activated primary human T cells had significantly higher [^{18}F]F-AraG uptake compared with resting T cells at all time points examined (***, $P < 0.001$; $n = 4$ per cell state per time point). Data in all graphs are expressed as mean ± SD.

donor T cells) and aGVHD (irradiated and bone marrow–transplanted mice with Luc$^+$ donor T cells) mice. Consistent with previous results (11, 24, 25) and based on a standard scoring system (30), both day 3 and day 10 mice in this model are considered within the T-cell activation phase of the disease. Day 3 aGVHD mice lack noticeable symptoms and are at a time point when T-cell activation is being initiated, whereas day 10 mice display clinical symptoms and are considered at the peak of T-cell activation. As previously demonstrated (11, 24, 25), *in vivo* BLI of aGVHD mice revealed that donor T cells at day 3 had accumulated preferentially in lymphoid organs such as the spleen, MLNs, and CLNs (Fig. 2A). On separate cohorts of mice receiving GFP$^+$ donor T cells, we qualitatively confirmed progressively higher donor T-cell accumulation within the spleen and CLN from days 3 to 10 (Supplementary Fig. S11). We also demonstrate that the percentage of donor T cells that are proliferating (Ki67$^+$)—a marker of activation—is higher at later (day 9) versus earlier time points (day 3; Supplementary Fig. S12). Importantly, [^{18}F]F-AraG PET/CT images taken 1 hour after tracer (~200 μCi) administration showed qualitatively higher uptake in the CLN in aGVHD versus control mice (Fig. 2B). Quantitative image analysis corroborated our findings revealing significantly higher (~1.4-fold) [^{18}F]F-AraG uptake in the CLNs of aGVHD mice ($P < 0.05$; Fig. 2C). At 1 hour, tracer uptake within abdominal organs such as the liver and kidneys obscured the ability to visualize *in vivo* differences in tracer accumulation within the MLN and spleen (Fig. 2B). However, tracer biodistribution studies assessed at 90 minutes after intravenous tracer injection revealed significantly higher [^{18}F]F-AraG accumulation in both the CLN ($P < 0.05$; ~2.3-fold) and the MLN ($P < 0.05$; ~2.0-fold), and a trend toward higher uptake in the spleen ($P = 0.12$; Fig. 2D). No significant differences were noted across all other organs between control and aGVHD mice. Thus, at an early stage of disease development prior to clinical symptoms in this model, [^{18}F]F-AraG accumulated in lymphoid organs (MLN, CLN, and spleen) harboring activated T cells and [^{18}F]F-AraG PET imaging enabled visualization of early T-cell accumulation within the CLN. At day 10, when donor T cells are highly proliferative (Supplementary Fig. S12), BLI revealed significantly higher total body signal compared with that in day 3 ($P < 0.01$; Supplementary Fig. S13), and qualitatively higher signal in the CLN region (Fig. 3A vs. Fig. 2A, and Supplementary Fig. S13; note differences in image scale). [^{18}F]F-AraG PET/CT images showed an even more apparent increase in tracer accumulation in the CLN of aGVHD compared with control mice (Fig. 3B), which was quantitatively confirmed via PET image analysis (Fig. 3C). Tracer biodistribution analysis revealed significantly lower

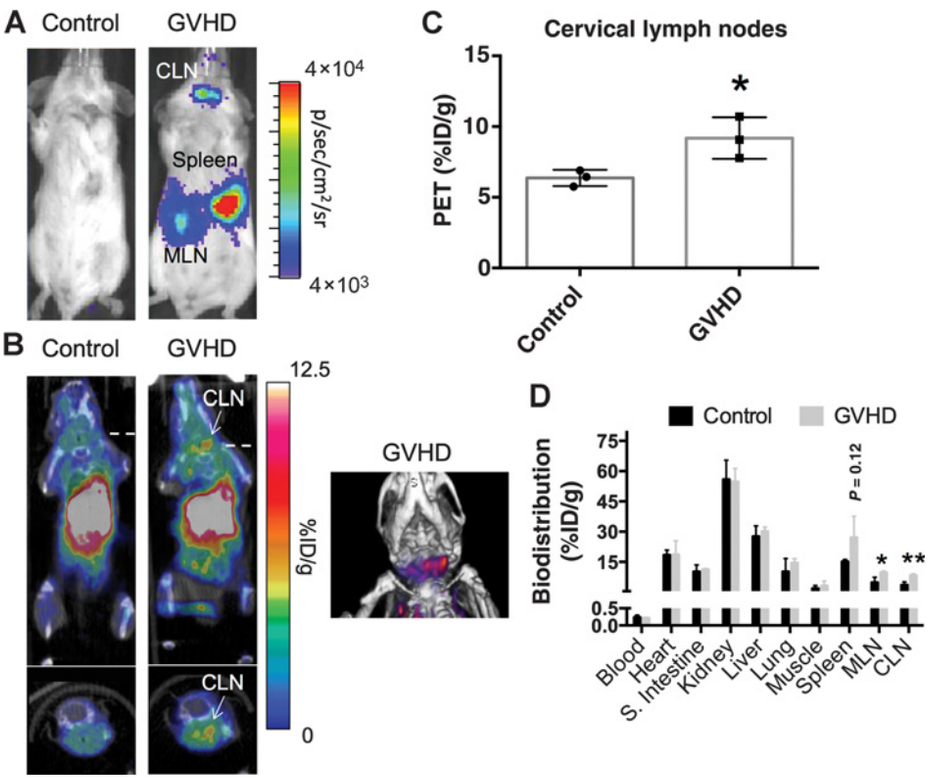

Figure 2.

Bioluminescence and [^{18}F]F-AraG PET imaging of donor T-cell dynamics during the initiation of T-cell activation in a mouse model of acute GVHD. **A,** BLI of control and GVHD mice 3 days after HCT revealed homing of luciferase-positive donor T cells to secondary lymphoid organs such as the spleen, CLNs, and MLNs in GVHD mice. **B,** Representative [^{18}F]F-AraG PET/CT images (10-minute static scan; 60–70 minutes post-tracer administration; ~200 μCi) at this time point showed visibly higher tracer uptake in the CLN of GVHD mice versus control mice ($n = 3$ per group). **C,** Quantitative region of interest PET image analysis of the CLN corroborated our qualitative assessments, demonstrating significantly (*, $P < 0.05$) higher tracer uptake in the CLN of GVHD mice versus control mice (%ID/g; percentage injected dose per gram of tissue). **D,** Biodistribution studies (90 minutes after tracer administration) also supported our imaging findings showing significantly (*, $P < 0.05$) higher tracer uptake in CLNs in GVHD versus control mice. Significantly (*, $P < 0.05$) higher tracer uptake was also apparent in the T cells harboring MLN, and a trend ($P = 0.12$) toward higher uptake was seen in the spleen. Data in all graphs are expressed as mean ± SD.

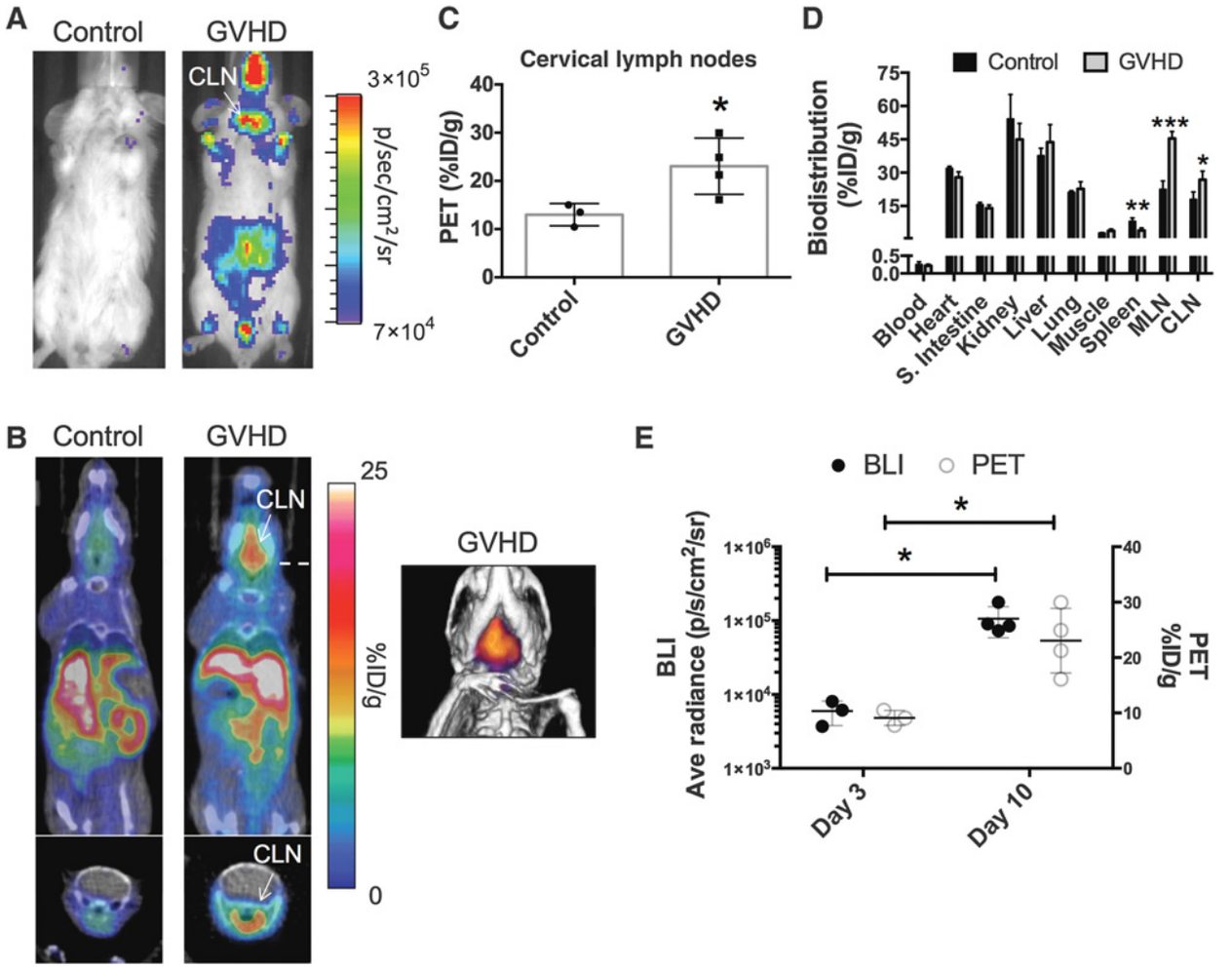

Figure 3.

Bioluminescence and [^{18}F]F-AraG PET imaging of donor T-cell dynamics during the peak of T-cell activation in a mouse model of acute GVHD. **A,** BLI of control and GVHD mice 10 days after HCT revealed more widespread distribution of luciferase-positive donor T cells in GVHD mice, but still localized accumulation within the CLNs. Note the order of magnitude difference in scale between the images shown here and those in Fig. 2A (day 3 after cell transplantation). **B,** Representative [^{18}F]F-AraG PET/CT images (10-minute static scans, 60–70 post-tracer administration; ~200 μCi) at this time point showed visibly higher tracer uptake in the CLN of GVHD ($n = 4$) versus control mice ($n = 3$). **C,** Quantitative region of interest PET image analysis of the CLN corroborated our qualitative assessments, demonstrating significantly higher tracer uptake in the CLN of GVHD versus control mice (*, $P < 0.05$; %ID/g; percentage injected dose per gram of tissue). **D,** Biodistribution studies (90 minutes after tracer administration) also supported our imaging findings, showing significantly higher tracer uptake in CLNs in GVHD versus control mice. Significantly higher tracer uptake was also apparent in the MLN (*, $P < 0.05$). At this time point, significantly lower tracer uptake was noted within the spleen (*, $P < 0.05$). **E,** Comparison of day 3 and day 10 bioluminescence and PET image analysis of CLNs shows both significantly higher BLI and PET signals on day 10 compared with day 3. Data in all graphs are expressed as mean ± SD.

tracer uptake in the spleen at this time point ($P < 0.05$), but higher uptake in both the CLN and the MLN ($P < 0.05$ and $P < 0.01$, respectively; Fig. 3D). Among aGVHD mice, we also showed significantly higher BLI and PET signal within the CLNs at day 10 versus day 3 ($P < 0.05$; Fig. 3E), indicating promise for monitoring disease burden via this surrogate imaging biomarker.

To further explore the suitability of [^{18}F]F-AraG for human studies, [^{18}F]F-AraG PET/CT scans were performed on six healthy human volunteers (Fig. 4). [^{18}F]F-AraG exhibited hepatobiliary and renal clearance with highest uptake in associated organs with SUV mean values (normalized to body weight) of 13.47 ± 1.46, 20.72 ± 5.26, and 17.27 ± 4.19 in liver, right, and left kidneys, respectively, at 47 to 77 minutes after tracer injection (Supplementary Table S1). High uptake was also observed in the myocardium as seen in mice, whereas relatively low background was observed in the thorax and lower abdomen. No significant adverse events or blood lab changes were observed due to tracer administration in any of the volunteers other than slightly increased urine esterase levels. Radiation dosimetry results are shown in Supplementary Table S2.

Discussion

aGVHD is a T-cell-mediated disease and the major complication of allogeneic HCT. aGVHD diagnosis is predominantly based on clinical symptoms, is often one of exclusion, and is typically

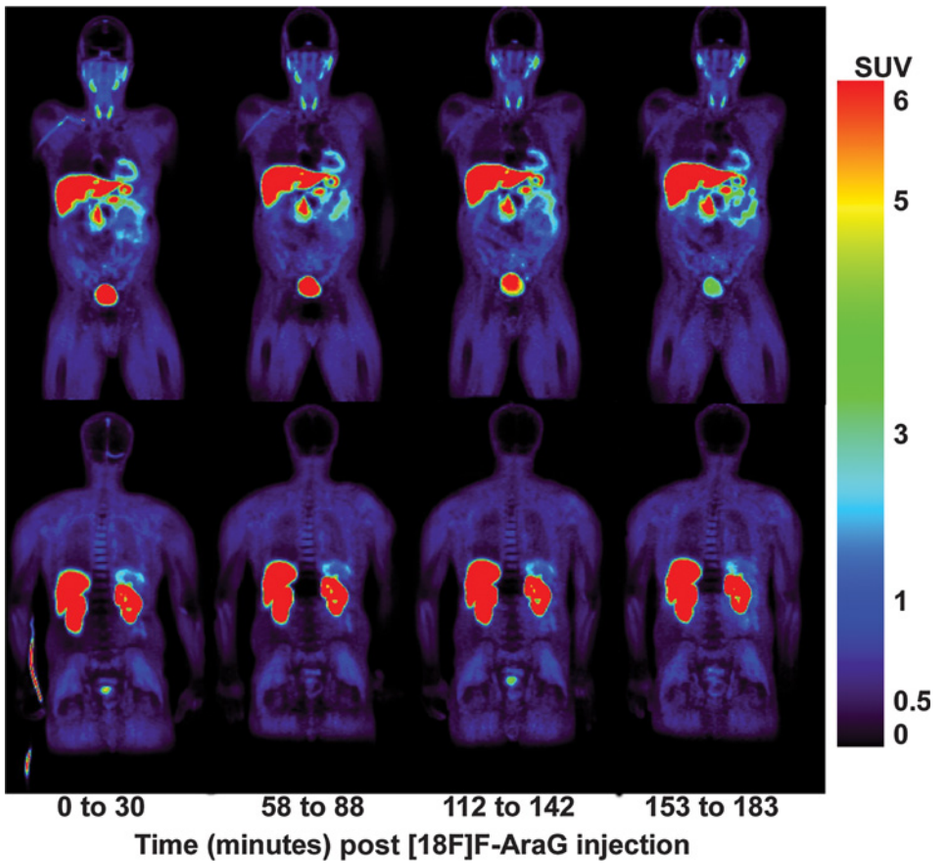

Figure 4.
Whole body PET images of [^{18}F]F-AraG in a healthy human volunteer. Frontal (top) and dorsal (bottom) coronal PET images taken immediately after intravenous injection of the tracer and at serial time points in one of the six humans imaged. Highest activity is observed in the liver, kidneys, and bladder, associated with [^{18}F]F-AraG clearance from the body. Uptake is also observed in the heart and spleen, whereas relatively low background activity is observed in all other tissues. Similar images were obtained from the other five subjects.

confirmed with invasive biopsies that have their own complications. Work on diagnostic blood assays has identified biomarkers, but more work needs to be done to validate these in multicenter prospective studies prior to widespread clinical use (31). Moreover, although noninvasive conventional imaging has played a role in aGVHD management, the structural manifestations that are detectable often only present at the latest of disease stages (32, 33). Molecular imaging of aGVHD, which may yield more sensitive detection, has been very limited, mostly focusing on PET imaging using [^{18}F]FDG (34), a nonspecific tracer with high uptake in many cell types and conditions. Overall, there is still no established single blood or imaging biomarker that is used for early diagnosis of aGVHD. A translationally relevant molecular imaging method that can noninvasively visualize activated T-cell dynamics within living subjects could enable earlier definitive aGVHD diagnosis and quantitative risk stratification to permit more timely and effective interventional strategies. Here, we show that, like the T-cell–specific cytotoxic drug AraG, the PET tracer [^{18}F]F-AraG is a substrate for cellular dCK and dGK activity, preferentially accumulates in both murine and human activated versus resting T cells, and [^{18}F]F-AraG PET imaging allowed quantitation of progressively increasing alloreactive T-cell accumulation in the CLN of aGVHD mice. Thus, this technology is an exciting new tool with high translational potential that can enable activated T-cell imaging in aGVHD mice and could be the missing link for earlier detection of this devastating disease.

Inclusive of aGVHD, selective noninvasive imaging of particular immune cell populations would have broad applicability in both immune-based disease detection and immunotherapy monitoring. Along these lines, the PET tracer [^{18}F]F-AraC was previously developed by screening deoxynucleoside analogs for preferential uptake in activated versus resting T cells (13). However, as with AraC, the selectivity of [^{18}F]F-AraC for accumulation in activated T cells *in vivo* is less than ideal (13). It is also subject to rapid *in vivo* deamination via cytidine deaminase activity, and although newer tracers avoiding this issue are being pursued (35, 36), the primary applications being pursued for [^{18}F]F-AraC are now tumor imaging. In contrast to AraC, AraG has shown remarkably selective cytotoxic effects toward T-lymphoblastoid cells and T lymphocytes compared with other immune cell lineages (17–19). Based on this knowledge, we previously described the chemical synthesis of the PET tracer [^{18}F]F-AraG in an attempt to develop a more selective activated T-cell molecular imaging probe (16). Here, we describe detailed mechanistic studies and *in vivo* imaging of [^{18}F]F-AraG in a relevant T-cell–mediated disease model. This is important as our tracer is a fluorinated version of AraG, and even though studies have shown that F-AraG behaves similarly to AraG (37), this may not have held true at low tracer concentrations. Our results in cultured cells support similar mechanisms of uptake and cell specificity as AraG because our tracer was preferentially retained in T-cell lines versus other immune cell lineages (17–19, 28), a competition assay with excess AraG-inhibited uptake of our tracer across all immune cell lines, and our tracer utilizes both dCK and dGK activities to accumulate into cells (21). dGK utilization is supported by our biodistribution

results in mice and humans showing moderately high tracer accumulation in the liver and heart, two organs with high dGK expression (38). Unlike AraC and [^{18}F]F-AraC, which are solely phosphorylated by dCK (13), AraG and [^{18}F]F-AraG are substrates for both dCK and dGK activities, with dCK described as a low-affinity, high specific activity enzyme and dGK as a high-affinity, low specific activity enzyme. The K_M of [^{3}H]AraG for dGK and dCK are 10 and 100 μmol/L, respectively (21), and thus our tracer at low nmol/L doses should preferentially utilize the dGK pathway, if available. However, dCK appears to be playing a significant role in [^{18}F]F-AraG uptake as loss of dCK in the T-lymphoblast cell line (CCRF-CEM) resulted in significantly lower intracellular levels (Fig. 1). The distinct mechanisms of uptake of [^{18}F]F-AraG compared with [^{18}F]F-AraC (i.e., dGK phosphorylation) is also supported by the differences in the uptake and efflux of both tracers across immune cell lines, solid tumor cell lines, and resting and primary activated T cells. Biodistribution in humans is also different between the two tracers with [^{18}F]F-AraC showing low liver and high splenic uptake (36), whereas [^{18}F]F-AraG showed high liver and moderate splenic uptake. Overall, our data strongly support the uniqueness of our tracer for imaging cell populations with high dCK and dGK activity including activated T cells.

Based on studies in the same mouse model we used here, aGVHD has two phases of disease progression called the activation phase and effector phase (11, 24, 25, 39). From an early diagnostic perspective, it would be ideal if subjects at risk for high-grade GVHD could be identified during the activation phase to fortify immunosuppressive therapy. Several candidate blood biomarkers have shown promise for early detection of aGVHD including a panel of proteomic blood biomarkers capable of diagnosis approximately 15 days before definitive diagnosis (10). Cellular biomarkers of aGVHD in the blood have also been explored. Bauerlein and colleagues have shown that, during their migration to effector organs, peripheral blood detection of alloreactive T cells expressing homing receptors ($\alpha4\beta7$ integrin and P-selectin ligand) can be used to define a diagnostic window for the improved treatment of aGVHD (11). We believe that [^{18}F]F-AraG PET imaging that can quantify activated T-cell accumulation within the CLN during the activation phase may provide a complementary technique to these blood-based diagnostics to provide more definitive early aGVHD diagnosis. Hypothetically, [^{18}F]F-AraG PET may even enable earlier diagnosis than a blood-based strategy by detection of T cells in priming sites prior to migration of cells or shedding of cellular proteins into the peripheral blood—a hypothesis that we are currently testing.

Several other imaging techniques have also shown promise for definitive diagnosis of aGVHD, particularly gastrointestinal manifestations of the disease, including MRI, CT, high-resolution transabdominal ultrasound, and color Doppler ultrasound (32, 33). These techniques primarily focus on detection of edema and thickening of the intestinal wall during advanced stages of aGVHD, and are therefore likely limited for early disease detection. [^{18}F]FDG PET has also shown promise for imaging intestinal inflammation associated with aGVHD in both mouse models and patients with early clinical symptoms, even allowing prediction and monitoring of therapy response in these patients (34). However, the utility of [^{18}F]FDG PET imaging for early detection prior to clinical symptoms is not known, and the nonspecific nature of [^{18}F]FDG imaging for a variety of activated immune cell types should enable a selective advantage of [^{18}F]F-AraG PET imaging for this purpose.

Despite the high sensitivity of PET imaging for low levels of molecular targets, it remains a challenge to detect scarce target cell numbers in small organs or organs near areas of nonspecific tracer accumulation (i.e., areas with high background signal). There is inherently a limit to the spatial resolution and cellular sensitivity that is achievable with PET. One limitation of our study was the inability to visualize *in vivo* differences of tracer uptake in both the MLN and spleen, two organs we know harbor activated donor T cells. Although our tracer *ex vivo* biodistribution results supported higher uptake in the MLN of aGVHD versus control mice at both early and late stages of disease, we were unable to identify the MLN in our PET (or CT) images. This was mostly due to high tracer uptake in adjacent organs such as the kidneys and liver at 1 hour after tracer administration. Although this is problematic in mice due to their small size and closely positioned organs, we believe this will be less of a concern in humans as supported by the low tracer uptake in the GI tract in human PET images of normal volunteers. The spleen showed an interesting pattern of tracer uptake in *ex vivo* biodistribution analysis with a trend toward higher tracer uptake in GVHD versus control mice at day 3 and significantly lower uptake at day 10. This contrasts with the data supporting more donor T cells in the spleen at day 10 compared with day 3. Although the reason for these differences is being actively investigated, the spleen has a more heterogeneous cellular composition than lymph nodes with T cells constituting a minor portion of this, so changes in overall cell composition or numbers may result in differences in tracer uptake as the disease progresses. We also found significantly decreased splenic weights between aGVHD and control mice at day 10 (0.06 ± 0.01 vs. 0.12 ± 0.01; $P < 0.01$). This suggests that at day 10, the spleen of GVHD mice may have been a site of extensive tissue damage, resulting in a lower absolute number of splenocytes (which may also take up the tracer at low levels), and lower overall tracer accumulation. We do see some tracer uptake in the spleen in human PET images so it will need to be determined whether [^{18}F]F-AraG accumulates in this organ at higher or lower levels in GVHD patients. As with dCK-targeted radiotracers (36), we are also actively pursuing alternative radioactive AraG analogs that may have different pharmacokinetic profiles.

In conclusion, we have shown that [^{18}F]F-AraG PET imaging may provide crucial information to aid in the detection of activated T-cell dynamics during the activation phase of aGVHD. Future work will focus on monitoring the effects of novel immunosuppressive therapies in this model. In addition, the preliminary studies in healthy human volunteers have been promising with low background in the thorax and GI tract, making it favorable for thoracic and pelvic imaging. Favorable kinetics of [^{18}F]F-AraG in humans along with the preclinical data support its potential as a promising tracer for early detection of GVHD and warrant its further clinical evaluation in aGVHD patients. Continued development of [^{18}F]F-AraG as a selective T-cell imaging agent in HCT patients is ongoing. Considering the paucity of activated T-cell PET tracers in the clinic, this work also lays the foundation for future use of [^{18}F]F-AraG PET for visualizing other T-cell–mediated diseases (e.g., multiple sclerosis, rheumatoid arthritis, Type 1 diabetes mellitus, etc.), evaluating endogenous

T-cell dynamics during the pathogenesis of other diseases (e.g., cancer or infection), and monitoring the effectiveness of T-cell–based immunotherapies.

Disclosure of Potential Conflicts of Interest

S.S. Yaghoubi and S.S. Gambhir have ownership interest (including patents) in CellSight Technologies, Inc. No potential conflicts of interest were disclosed by the other authors.

Authors' Contributions

Conception and design: J.A. Ronald, B.-S. Kim, M. Namavari, J. Baker, S.S. Yaghoubi, H.F. VanBrocklin, B.L. Franc, J. Benjamin, R. Negrin, S.S. Gambhir
Development of methodology: J.A. Ronald, B.-S. Kim, G. Gowrishankar, M. Namavari, O. Ilovich, A. Hoehne, J. Baker, S.S. Yaghoubi, B.L. Franc, S. Jivan, J.B. Slater, J. Benjamin, S.S. Gambhir
Acquisition of data (provided animals, acquired and managed patients, provided facilities, etc.): J.A. Ronald, B.-S. Kim, G. Gowrishankar, A. D'Souza, H. Nishikii, H.-Y. Chuang, O. Ilovich, C.-F. Lin, R. Reeves, A. Shuhendler, C.T. Chan, J. Baker, S.S. Yaghoubi, H.F. VanBrocklin, R. Hawkins, B.L. Franc, E.F. Verdin, K.T. Gao
Analysis and interpretation of data (e.g., statistical analysis, biostatistics, computational analysis): J.A. Ronald, B.-S. Kim, I.S. Alam, H. Nishikii, J. Baker, S.S. Yaghoubi, H.F. VanBrocklin, R. Hawkins, B.L. Franc, R. Negrin, S.S. Gambhir
Writing, review, and/or revision of the manuscript: J.A. Ronald, B.-S. Kim, I.S. Alam, H. Nishikii, O. Ilovich, A. Shuhendler, C.T. Chan, J. Baker, S.S. Yaghoubi, H.F. VanBrocklin, R. Hawkins, B.L. Franc, K.T. Gao, R. Negrin, S.S. Gambhir
Administrative, technical, or material support (i.e., reporting or organizing data, constructing databases): I.S. Alam, C.-F. Lin, R. Reeves, A. Hoehne, R. Hawkins, B.L. Franc, J.B. Slater, E.F. Verdin, K.T. Gao, S.S. Gambhir
Study supervision: S.S. Yaghoubi, R. Hawkins, S.S. Gambhir

Acknowledgments

The authors would like to acknowledge the support of the Stanford Center for Innovation in In-Vivo Imaging (SCI^3) for all preclinical imaging experiments and Dr. Frezghi Habte for help with PET image analysis. We would also like to thank Dr. Beverly Mitchell (Stanford University) for providing the dCK^- cell line, Dr. Varsha Gandhi (MD Anderson) for providing the dCK^+ and dGK^+ cell lines, and Dr. Heike Daldrup-Link (Stanford University) for providing the PyMT cell line. We are also grateful to Xinrui Yan for supporting the preclinical studies, Samuel Quezada (Cellsight Technologies) for supporting clinical studies, and Mirwais Wardak for insightful comments on the article. We acknowledge the assistance of Vahid Ravanfar acquiring the patient images on the GE PET/MR.

Grant Support

This work was funded by several grants including NCI ICMIC P50CA114747 (S.S. Gambhir), NCI RO1 R01CA201719 (S.S. Gambhir), Ben & Catherine Ivy Foundation (S.S. Gambhir), and Phase II SBIR Contract HHSN261201300063C (S.S. Yaghoubi).

The costs of publication of this article were defrayed in part by the payment of page charges. This article must therefore be hereby marked *advertisement* in accordance with 18 U.S.C. Section 1734 solely to indicate this fact.

Received October 28, 2016; revised December 7, 2016; accepted March 31, 2017; published online June 1, 2017.

References

1. McDonald-Hyman C, Turka LA, Blazar BR. Advances and challenges in immunotherapy for solid organ and hematopoietic stem cell transplantation. Sci Transl Med 2015;7:280rv2.
2. Gratwohl A, Brand R, Frassoni F, Rocha V, Niederwieser D, Reusser P, et al. Cause of death after allogeneic haematopoietic stem cell transplantation (HSCT) in early leukaemias: An EBMT analysis of lethal infectious complications and changes over calendar time. Bone Marrow Transplant 2005;36:757–69.
3. Ferrara JLM, Levine JE, Reddy P, Holler E. Graft-versus-host disease. Lancet 2009;373:1550–61.
4. Tabbara IA, Zimmerman K, Morgan C, Nahleh Z. Allogeneic hematopoietic stem cell transplantation: Complications and results. Arch Intern Med 2002;162:1558–66.
5. Ferrara JL, Deeg HJ. Graft-versus-host disease. N Engl J Med 1991;324:667–74.
6. Jamani K, Russell JA, Daly A, Stewart D, Savoie L, Duggan P, et al. Prognosis of grade 3–4 acute GVHD continues to be dismal. Bone Marrow Transplant 2013;48:1359–61.
7. Przepiorka D, Weisdorf D, Martin P, Klingemann HG, Beatty P, Hows J, et al. 1994 Consensus conference on acute GVHD grading. Bone Marrow Transplant 1995;15:825–8.
8. Malard F, Mohty M. New insight for the diagnosis of gastrointestinal acute graft-versus-host disease. Mediators Inflamm 2014;2014:701013.
9. Vogelsang GB, Lee L, Bensen-Kennedy DM. Pathogenesis and treatment of graft-versus-host disease after bone marrow transplant. Annu Rev Med 2003;54:29–52.
10. De Bock M, Beguin Y, Leprince P, Willems E, Baron F, Deroyer C, et al. Comprehensive plasma profiling for the characterization of graft-versus-host disease biomarkers. Talanta 2014;125:265–75.
11. Bäuerlein CA, Riedel SS, Baker J, Brede C, Garrote A-LJ, Chopra M, et al. A diagnostic window for the treatment of acute graft-versus-host disease prior to visible clinical symptoms in a murine model. BMC Med 2013;11:134.
12. James ML, Gambhir SS. A molecular imaging primer: Modalities, imaging agents, and applications. Physiol Rev 2012;92:897–965.
13. Radu CG, Shu CJ, Nair-Gill E, Shelly SM, Barrio JR, Satyamurthy N, et al. Molecular imaging of lymphoid organs and immune activation by positron emission tomography with a new [18F]-labeled 2′-deoxycytidine analog. Nat Med 2008;14:783–8.
14. Di Gialleonardo V, Signore A, Glaudemans AWJM, Dierckx RAJO, de Vries EFJ. N-(4–18F-fluorobenzoyl)interleukin-2 for PET of human-activated T lymphocytes. J Nucl Med 2012;53:679–86.
15. Tavaré R, McCracken MN, Zettlitz KA, Knowles SM, Salazar FB, Olafsen T, et al. Engineered antibody fragments for immuno-PET imaging of endogenous CD8+ T cells in vivo. Proc Natl Acad Sci U S A 2014;111:1108–13.
16. Namavari M, Chang Y-F, Kusler B, Yaghoubi S, Mitchell BS, Gambhir SS. Synthesis of 2′-deoxy-2′-[18F]fluoro-9-β-D-arabinofuranosylguanine: a novel agent for imaging T-cell activation with PET. Mol Imaging Biol 2011;13:812–8.
17. Cohen A, Lee JW, Gelfand EW. Selective toxicity of deoxyguanosine and arabinosyl guanine for T-leukemic cells. Blood 1983;61:660–6.
18. Shewach DS, Daddona PE, Ashcraft E, Mitchell BS. Metabolism and selective cytotoxicity of 9-beta-D-arabinofuranosylguanine in human lymphoblasts. Cancer Res 1985;45:1008–14.
19. Shewach DS, Mitchell BS. Differential metabolism of 9-beta-D-arabinofuranosylguanine in human leukemic cells. Cancer Res 1989;49:6498–502.
20. Roecker AM, Stockert A, Kisor DF. Nelarabine in the treatment of refractory T-cell malignancies. Clin Med Insights Oncol 2010;4:133.
21. Rodriguez CO, Mitchell BS, Ayres M, Eriksson S, Gandhi V. Arabinosylguanine is phosphorylated by both cytoplasmic deoxycytidine kinase and mitochondrial deoxyguanosine kinase. Cancer Res 2002;62:3100–5.
22. Bauer C, Bauder-Wuest U, Mier W, Haberkorn U, Eisenhut M. 131I-labeled peptides as caspase substrates for apoptosis imaging. J Nucl Med 2005;46:1066–74.
23. Nakanishi T, Ross DD, Mitsuoka K. Methods to evaluate transporter activity in cancer. Totowa, NJ: Humana Press; 2010. p. 105–20.
24. Beilhack A, Schulz S, Baker J, Beilhack GF, Nishimura R, Baker EM, et al. Prevention of acute graft-versus-host disease by blocking T-cell entry to secondary lymphoid organs. Blood 2008;111:2919–28.
25. Beilhack A, Schulz S, Baker J, Beilhack GF, Wieland CB, Herman EI, et al. In vivo analyses of early events in acute graft-versus-host disease reveal sequential infiltration of T-cell subsets. Blood 2005;106:1113–22.
26. Cao Y-A, Wagers AJ, Beilhack A, Dusich J, Bachmann MH, Negrin RS, et al. Shifting foci of hematopoiesis during reconstitution from single stem cells. Proc Natl Acad Sci U S A 2004;101:221–6.

27. Kim BS, Nishikii H, Baker J, Pierini A, Schneidawind D, Pan Y, et al. Treatment with agonistic DR3 antibody results in expansion of donor Tregs and reduced graft-versus-host disease. Blood 2015;126:546–57.
28. Verhoef V, Fridland A. Metabolic basis of arabinonucleoside selectivity for human leukemic T- and B-lymphoblasts. Cancer Res 1985;45:3646–50.
29. Kim W, Le TM, Wei L, Poddar S, Bazzy J, Wang X, et al. [18F]CFA as a clinically translatable probe for PET imaging of deoxycytidine kinase activity. Proc Natl Acad Sci U S A 2016;113:4027–32.
30. Cooke KR, Kobzik L, Martin TR, Brewer J, Delmonte J, Crawford JM, et al. An experimental model of idiopathic pneumonia syndrome after bone marrow transplantation: I. The roles of minor H antigens and endotoxin. Blood 1996;88:3230–9.
31. Levine JE, Braun TM, Harris AC, Holler E, Taylor A, Miller H, et al. A prognostic score for acute graft-versus-host disease based on biomarkers: A multicentre study. Lancet Haematol 2015;2:e21–9.
32. Mentzel HJ, Kentouche K, Kosmehl H, Gruhn B, Vogt S, Sauerbrey A, et al. US and MRI of gastrointestinal graft-versus-host disease. Pediatr Radiol 2002;32:195–8.
33. Kalantari BN, Mortele KJ, Cantisani V, Ondategui S, Glickman JN, Gogate A, et al. CT features with pathologic correlation of acute gastrointestinal graft-versus-host disease after bone marrow transplantation in adults. AJR Am J Roentgenol 2003;181:1621–5.
34. Stelljes M, Hermann S, Albring J, Köhler G, Löffler M, Franzius C, et al. Clinical molecular imaging in intestinal graft-versus-host disease: Mapping of disease activity, prediction, and monitoring of treatment efficiency by positron emission tomography. Blood 2008;111:2909–18.
35. Shu CJ, Campbell DO, Lee JT, Tran AQ, Wengrod JC, Witte ON, et al. Novel PET probes specific for deoxycytidine kinase. J Nucl Med 2010;51:1092–8.
36. Schwarzenberg J, Radu CG, Benz M, Fueger B, Tran AQ, Phelps ME, et al. Human biodistribution and radiation dosimetry of novel PET probes targeting the deoxyribonucleoside salvage pathway. Eur J Nucl Med Mol Imaging 2011;38:711–21.
37. Montgomery JA, Shortnacy AT, Carson DA, Secrist JA. 9-(2-Deoxy-2-fluoro-β-D-arabinofuranosyl)guanine: A metabolically stable cytotoxic analogue of 2′-deoxyguanosine. J Med Chem 1986;29:2389–92.
38. Johansson M, Karlsson A. Cloning and expression of human deoxyguanosine kinase cDNA. Proc Natl Acad Sci U S A 1996;93:7258–62.
39. van Leeuwen L, Guiffre A, Atkinson K, Rainer SP, Sewell WA. A two-phase pathogenesis of graft-versus-host disease in mice. Bone Marrow Transplant 2002;29:151–8.